SUPPORTING INFORMATION

Bottom-up process of self-formation of highly conductive titanium oxide (TiO) nanowires on reduced $SrTiO_3$

Dominik Wrana, Christian Rodenbücher, Benedykt R. Jany, Oleksandr Kryshtal, Grzegorz Cempura, Adam Kruk, Paulina Indyka, Krzysztof Szot, Franciszek Krok*

1. Atomically resolved images of nanowires from Transmission Electron Microscopy (TEM)

Here we present a few high-resolution examples of TiO nanowires formed on $SrTiO_3$(100), imaged by means of atomically resolved transmission electron microscopy, in the scanning mode (STEM). Figure S1 shows the raw HAADF-STEM image from Figure 3 in the main text, to prove no defects were hidden by insets. Crystallographic structure seems to be nearly perfect (within the focal length of the imaging mode). No dislocations in the $SrTiO_3$ matrix are visible, which may be explained by the fact the lamella has the thickness of about 40 nm, which constitutes only approx.1/100 of the nanowire length. Figure S2 presents the HAADF (a) and ABF (b) images of another nanowire. The same zig-zag interface structure is visible, as well as the relative 4.6° tilt angle of $SrTiO_3$ and TiO crystal structures.

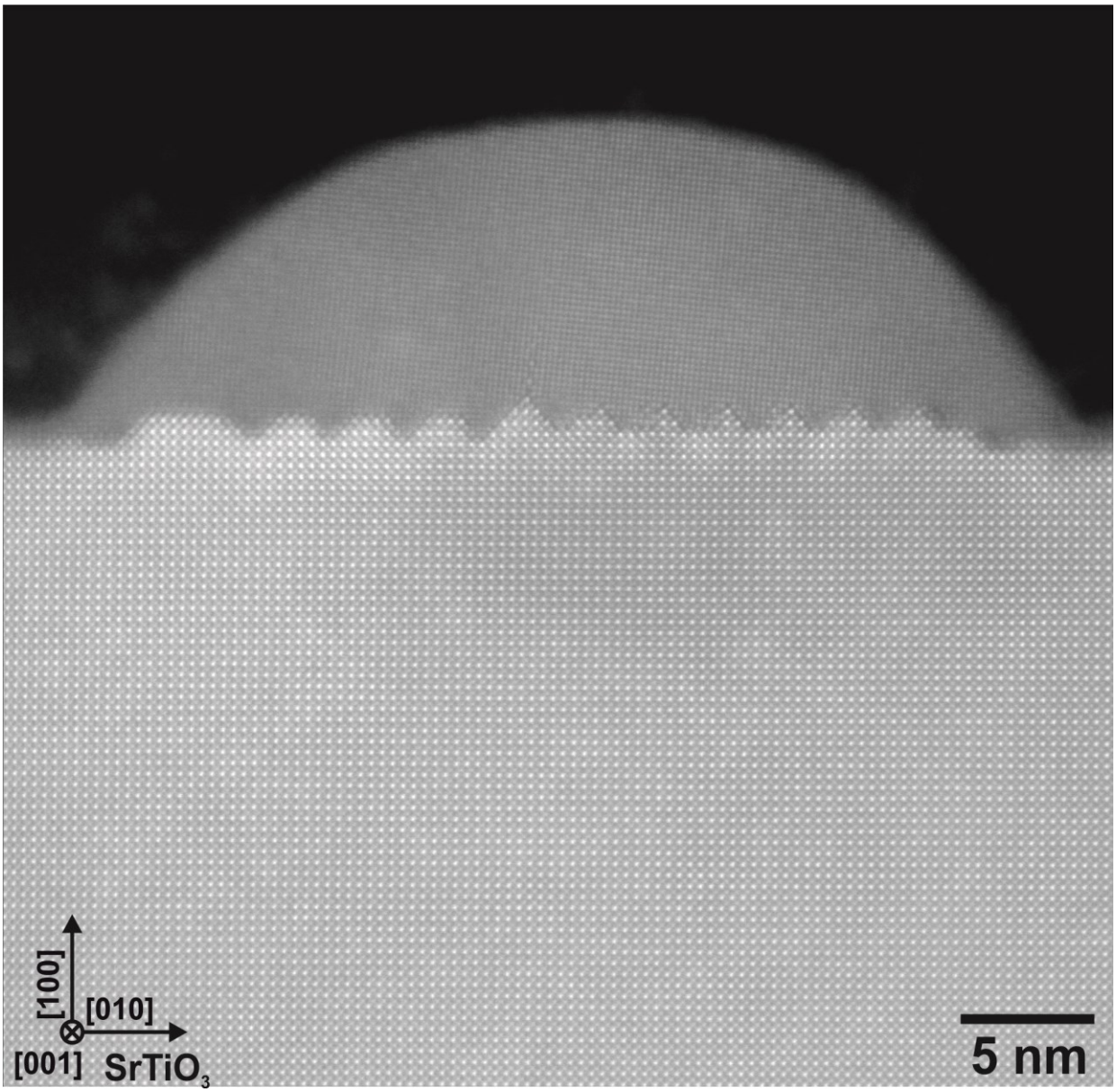

Figure S1. Atomically resolved HAADF-STEM image of a single TiO nanowire grown on $SrTiO_3$ surface (the same area which is displayed in Figure 3 in the main text).

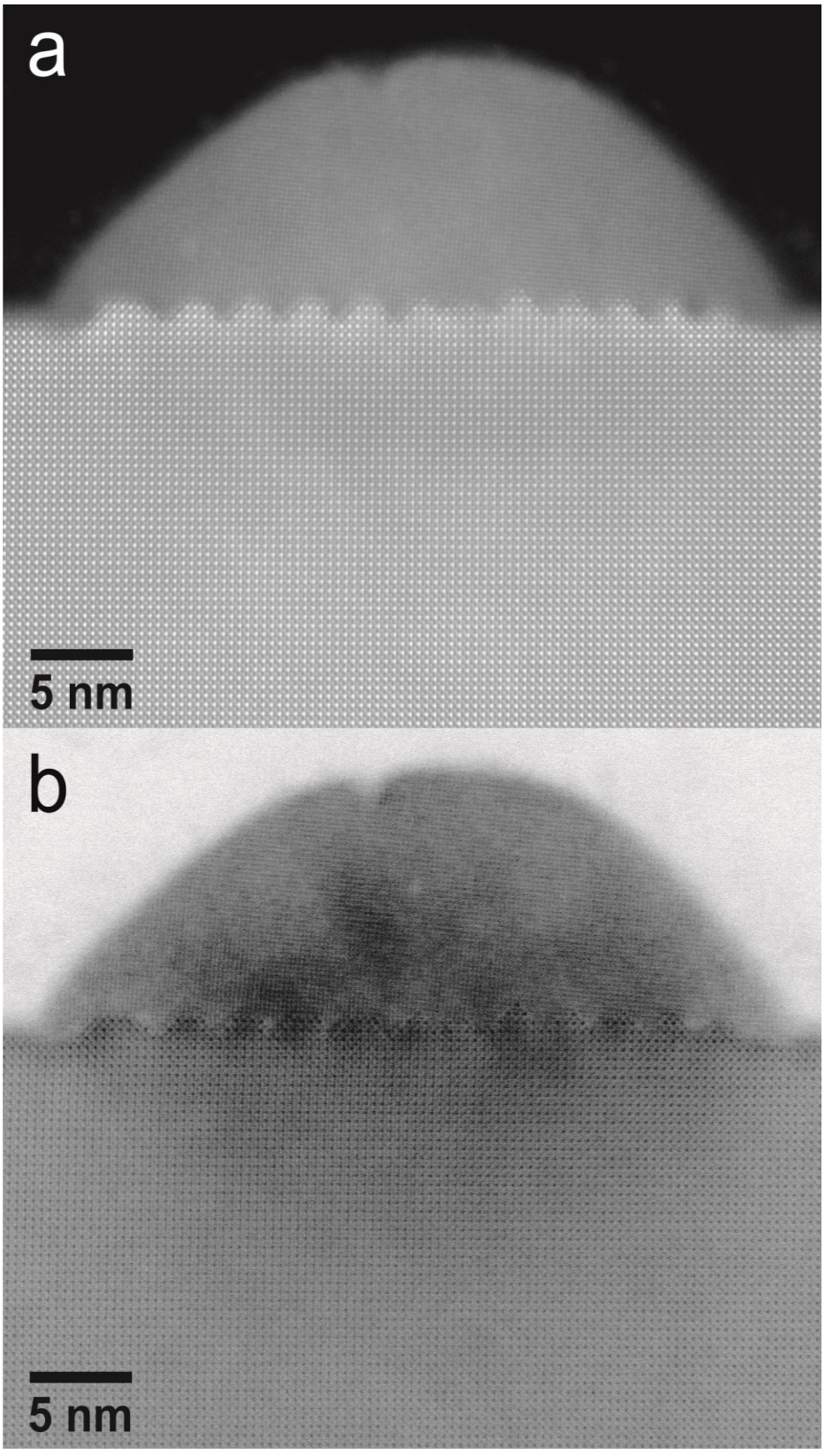

Figure S2. Atomically resolved STEM images of a single TiO nanowire grown on $SrTiO_3$ surface, taken at the [001] incidence. a) High Angle Annular Dark Field (HAADF-STEM) image. b) Annular Bright Field (ABF-STEM) image of the same island.

Figure S3 presents diffraction patterns collected by means of Nano Beam Diffraction technique in TEM. Smallest condenser aperture was used to obtain diffraction from areas of about 5 nm in diameter. Three distinguishable patterns were acquired: 1 – $SrTiO_3$ matrix underneath the nanowire, 2 – TiO nanowire, 3 – TiO/STO interface. Simulated diffraction patterns of perovskite $SrTiO_3$(001) and rock-salt TiO(001) crystal structures fitted perfectly to the acquired spots, proving that ELOP mechanism resulted in the formation of perfect TiO nanowires, maintaining the high crystallinity of the $SrTiO_3$ substrate. From the pattern collected at the TiO/STO interface the mutual angle of 4.6° was established.

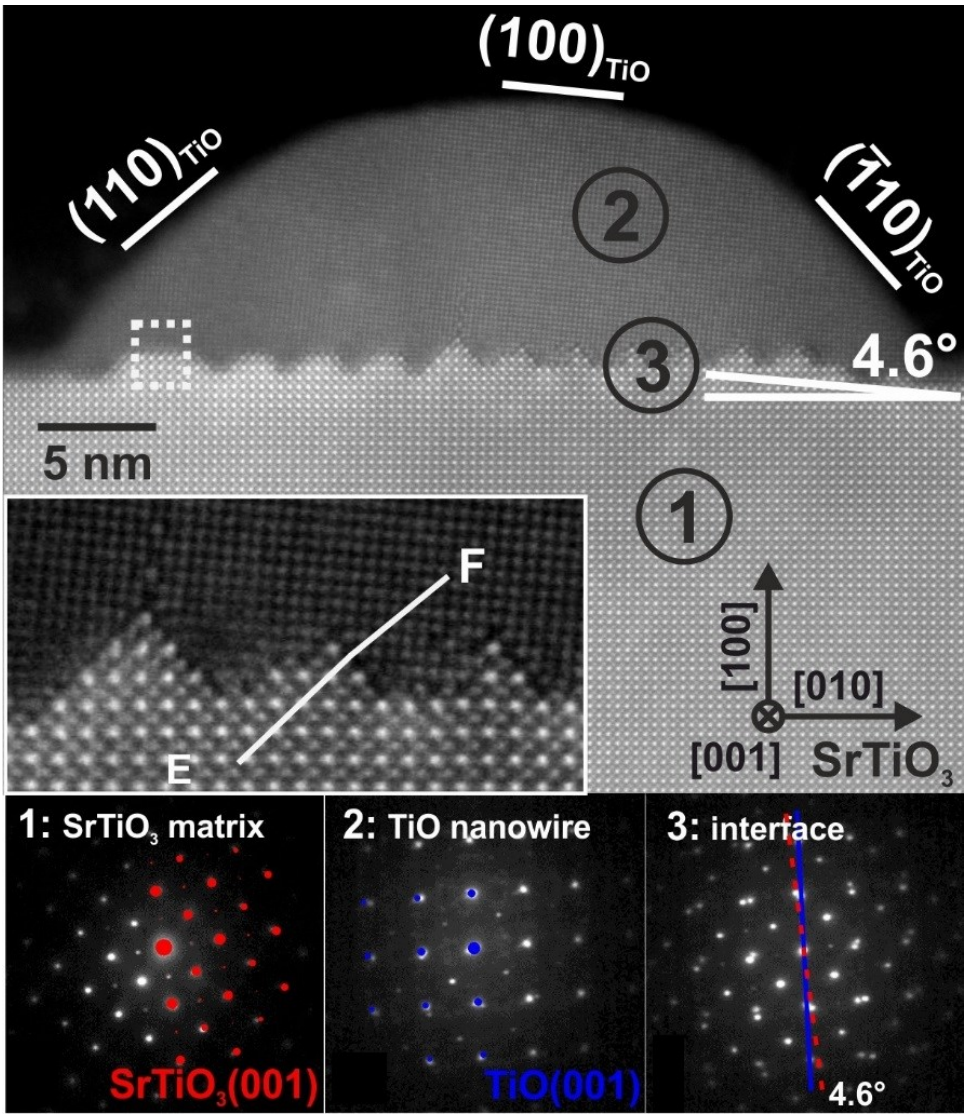

Figure S3. Nano-Beam Diffraction (NBD) patterns from three regions: 1 – $SrTiO_3$ matrix, 2 – TiO nanowire, 3 – interface. Theoretical diffraction patterns of $SrTiO_3$ and TiO are fitted, in red and blue respectively

2. Crystallographic texture of TiO nanowires on $SrTiO_3$

The crystallographic texture of reduced $SrTiO_3$ samples were characterized additionally via the Electron Backscatter Diffraction method (EBSD) in a SEM system equipped with the EDAX TSL DigiView camera. The aim of this investigation was to prove that all the formed nanowires have the same crystallographic structure, since TEM measurements allow only for a selective and limited characterization. The EBSD diffraction patterns were collected at a 70° sample tilt at 5 keV beam energy. The diffraction patterns were automatically indexed by EDAX TSL OIM DC 7.2.1 software, according to the perovskite phase of $SrTiO_3$ and the cubic rock-salt phase of TiO. The collected EBSD data were subject to clean-up algorithm procedures to ensure that reliable data were displayed, only data with CI>0.1 are shown. Figure S4 shows the results of the phase identification. Image Quality (IQ) as well as Phase map show inarguably that all the nanowires adopt different crystallographic structure than $SrTiO_3$ surface betwixt and between them. Inverse Pole Figure (IPF) map shown in Fig. S4 c proves that all of them aligned along main crystallographic directions ([001], [010] of $SrTiO_3$) have the same TiO rock salt structure. The tilt angle from the STO surface normal is about 4.6°, which stands in agreement with TEM images as well as TM-AFM investigations presented in the main text. IPF map of the STO surface proves that no structural transformations affect areas between nanowires and globally the surface has still the perovskite symmetry and the (100) orientation.

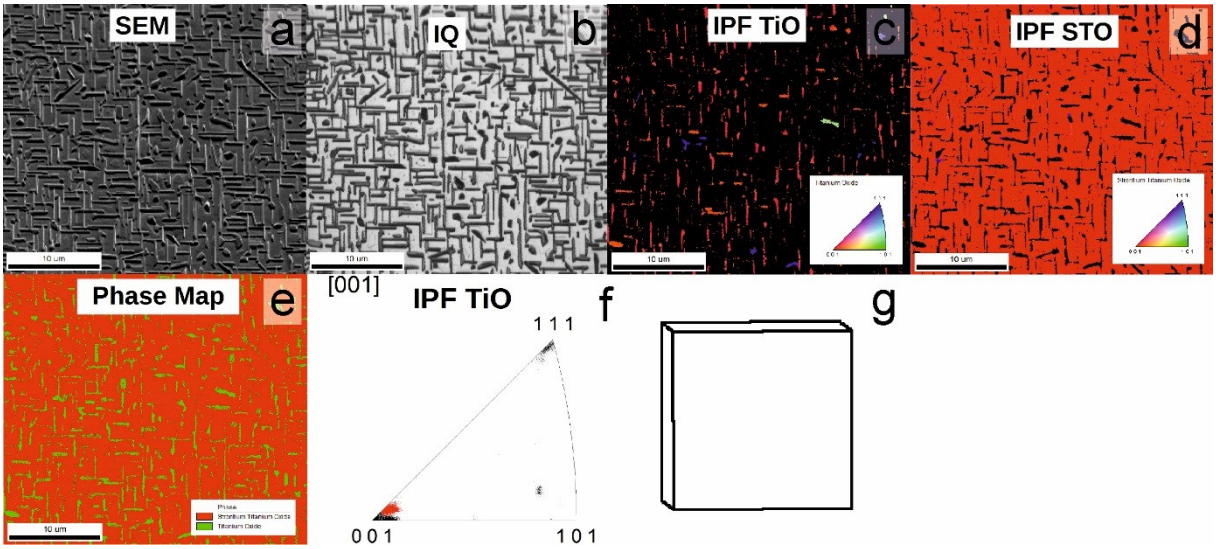

Figure S4. Crystallographic texture of TiO nanowires grown on $SrTiO_3$(100). a) Secondary electrons (SE) SEM image of a nanowire matrix, b) Image Quality (IQ) map of the same region, c) Inverse Pole Figure (IPF) map of TiO, obtained from EBSD, d) IPF map of STO, showing that the only STO orientation is still (100), e) Phase map with TiO nanowires marked in green and $SrTiO_3$ surface in red. f) IPF plot of TiO, showing that predominant orientation of nanowires is (001) with 4.6° tilt from the STO surface normal (marked in red), g)

Schematic representation of TiO crystallographic orientation with respect to the STO substrate.

3. Chemical imaging contrast

Most common imaging mode in the electron microscopy utilizes secondary electrons emitted from the surface, detected by use of the Everhart-Thornley detector. It allows for an effective measurements of surface topography, with hindered chemical contrast.

In contrary, backscatter electrons (BSE) mode is a powerful tool for the chemical analysis of the surface. The fraction of backscattered electrons is proportional to the atomic number Z of the elements in the material. Since we deal with three-elements system (Ti, Sr, O) where two cations have substantially different atomic numbers ($Z_{Sr} = 38$, $Z_{Ti} = 22$), one can distinguish between areas of different Ti/Sr ratio. Figure S5 presents the comparison of topographical (SE) and chemical (BSE) imaging of the network of TiO nanowires grown on $SrTiO_3$. Clearly nanowires have darker contrast in BSE, meaning the average Z number is lower. One can also estimate the TiO nanowires height from the BSE image, since there is a strong dependence of the probability of the backscattering electron on the depth. Table presented in Figure S5 contains the calculated BSE emission yields, using the CASINO software [1]. Assuming that areas between nanowires are pure STO (TiO thickness = 0 nm) and comparing the BSE intensities of nanowires and STO, the estimated average height of TiO is approx. 50 nm, which is in a good agreement with the measured height of nanowires at this region (by means of TM-AFM).

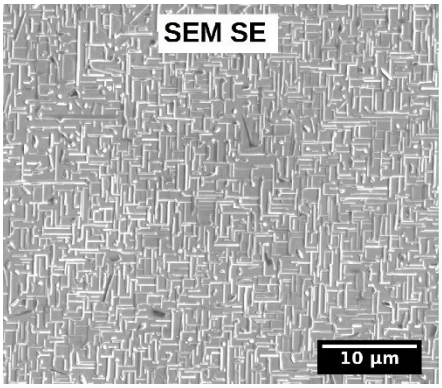

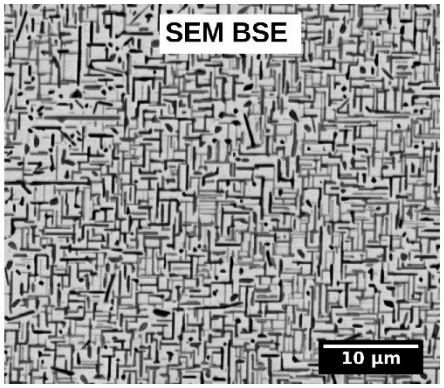

TiO thickness on STO	*BSE yield calculated by CASINO*
0 nm	0.2341
10 nm	0.2235
20 nm	0.2138
50 nm	0.1985
100 nm	0.1907
200 nm	0.1800

Figure S5. Comparison of Secondary Electrons (SE) and Backscattered Electrons (BSE) imaging contrast of TiO nanowires on $SrTiO_3$, collected at 5keV electron energy. Table

contains calculated (by the CASINO software) BSE emission yields of a thin TiO layer on $SrTiO_3$.

4. EELS spectra of TiO/$SrTiO_3$ interface

To determine actual chemical and valence composition at the interface between TiO nanowires and $SrTiO_3$ substrate, Electron Energy Loss Spectroscopy (EELS) scans in the STEM mode were performed. Energy loss near-edge structure (ELNES) provided information about the Ti and O electronic states and also geometrical structure. Although in both TiO and $SrTiO_3$ structures Ti atoms are surrounded by O atoms in the octahedral configuration, profound differences are expected due to the different bonding and therefore splitting of EELS spectra. Figure S6 shows line profile of a Ti L-edge across the TiO/$SrTiO_3$ interface. Sharp transition of a Ti ELNES spectrum is clearly visible. Titanium atoms in the TiO rocksalt structure have 2+ valence state, which is seen as two L_2 and L_3 peaks due to the Ti 2p spin-orbit splitting. For the case of Ti^{4+} in the $SrTiO_3$ interaction with a crystal field results in the removal of the degeneracy of Ti 2p levels and thus to the further splitting of $L_{2,3}$ into t_{2g} and e_g states. Moreover higher oxidation state of Ti in the STO region is also evident in the Ti-$L_{2,3}$ edge onset shift towards higher energy loss.

It is noteworthy that the shift of the TM onset value of the energy loss and the change in white-line intensity ratio (L_3/L_2) are two essential indicators of valence state modification. The EELS peak features of the O–K edges are more related to the geometry of the metal–oxygen bonding rather than the oxidation state, to which the transition metal is more sensitive [2][3].

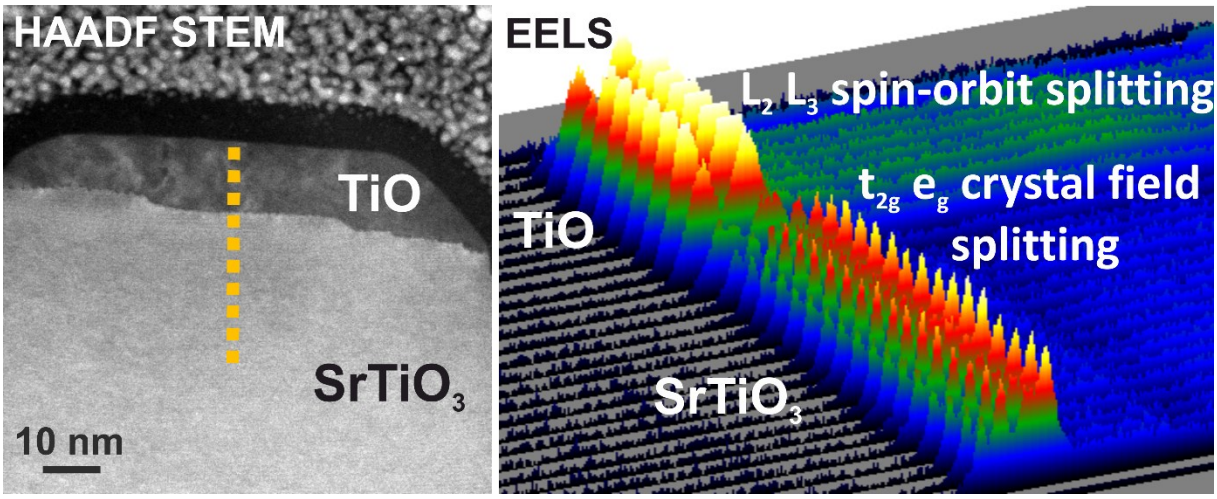

Figure S6. EELS line profile across the TiO/STO interface. Fine structure resolved at the ELNES Ti-$L_{2,3}$ edge shows evolution from Ti^{2+} at the nanowire to Ti^{4+} in the $SrTiO_3$ matrix.

More precise measurements reveal that the transition from Ti 2+ to 4+ valence state occurs within two unit cells (Fig S7). Additionally, Ti L-edge and O K-edge ELNES spectra are shown in a) and b) respectively. Ti spectra show clearly the two splitting processes mentioned before. In addition, positions of Ti L-edge peaks are in good agreement with the literature [4] indicating energy shifts attributed to changes of Ti oxidation state. Unaffected O-K position serves as a marker tool providing better control over the acquisition experiment assuring any drift of the spectrum is cancelled and observed effects of the Ti-$L_{2,3}$ range spectrum shifts are real. This is crucial while taking the average of the signal for many pixels (binning in the vertical direction) when it might happen that the spectrum is broaden due to the uncorrected drift. Significant differences in the oxygen K-edge for TiO and $SrTiO_3$ structures are visible in Fig. S7 b.

For the case of strontium titanate, a number of peaks can be attributed (A, B, C, D, E), coming from the titanium-oxygen interactions. The O K-edge in STO shows two intense peaks A and C with the suggestion of a less intense shoulder B, following by the peak D and less intense peak E.

In the simplest form, O K-edges represent electron transitions of the O 1s core level to the unoccupied p-like states [5]. It has been suggested that the peak A in TiO and A, B, C peak series in STO are due to oxygen 2p-metal 3d hybridization [6], and the main D peak in the O K-edge is thought to arise from hybridization of oxygen p-states with the TM 4s/d-states and continuum like states [7]. Peak E arises from higher lying energy states which can be most conveniently described in a scattering picture as resulting from scattering events in the first oxygen shell [4] being sensitive to the medium range order within the structure and so reveal any differences in the packing arrangements of oxygen anions.

Here (see Fig. S7 b), peak A corresponds to the transitions into unoccupied Ti 3d (t_{2g})–O 2p whereas less intense B peak represents-the unoccupied Ti 3d (e_g)–O 2p bands. Reduced intensity of a peak B may come from the geometrical reasons and reflect directionality of a Ti-O bonding at a specific oxygen site, from which EELS spectrum was acquired [8][9][10]. Here it seems that the high intensity of peak A and low intensity of peak B is more governed by the little or no change in symmetry rather than by the exchange splitting in the t_{2g}-e_g ligand field [6].

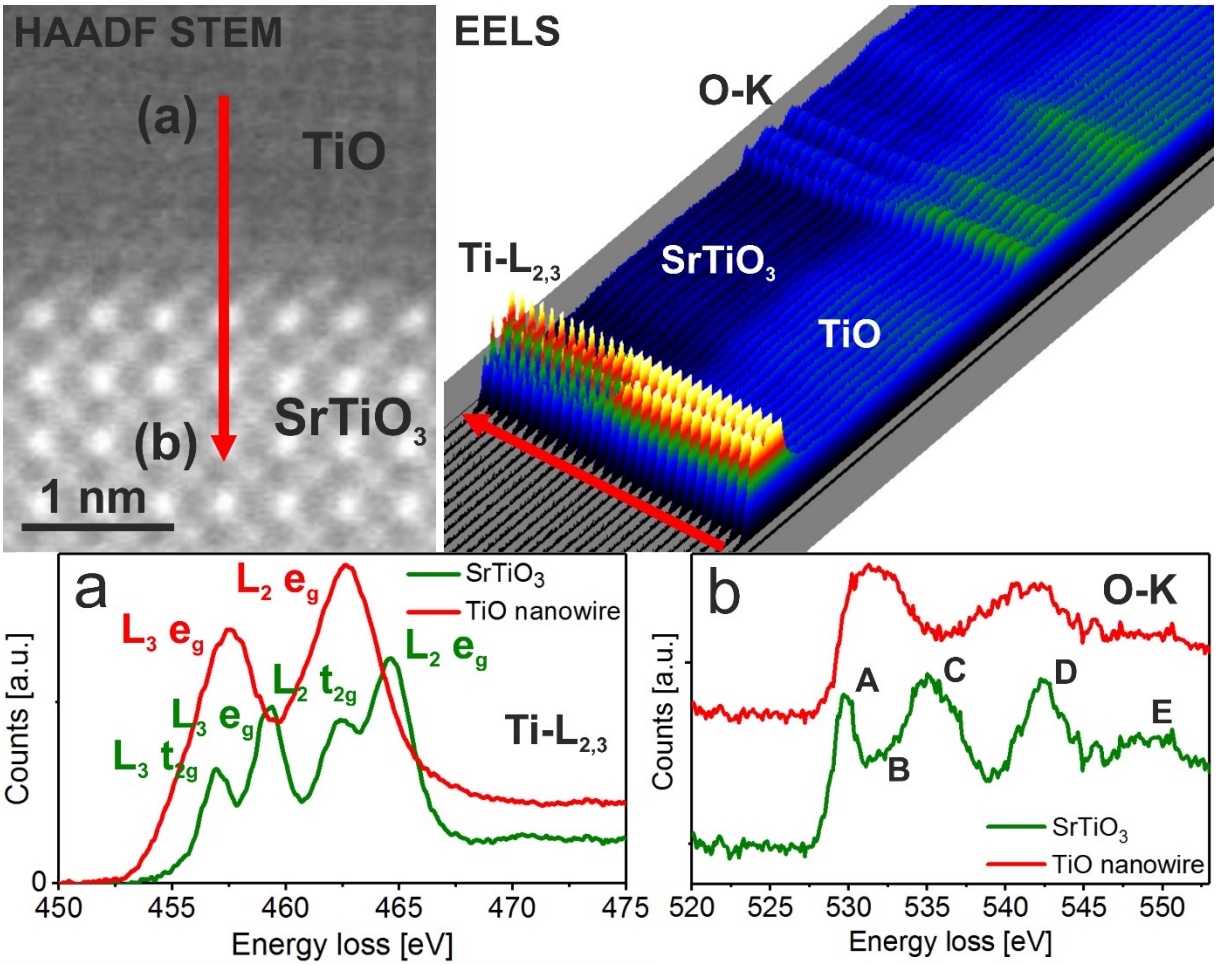

Figure S7. EELS profile at the TiO/STO interface, with the atomic precision. a) Ti L-edge ELNES acquired at the TiO nanowire and $SrTiO_3$ are compared. b) ELNES spectra of the O K-edge at the TiO and STO respectively.

5. Scalability of TiO nanowire networks

Utilizing the ELOP mechanism, one can produce TiO nanowire arrays covering macroscopic samples homogeneously. Maintaining stable reducing conditions (oxygen partial pressure, temperature of annealing) enables for the fabrication of macroscopic films of TiO with high surface area, for catalytic and energy storage applications. Figure S8 shows the uniform TiO nanowire network formed on the surface of $SrTiO_3$. The area covered by nanowires are even larger, however, the lower magnifications do not allow for a proper identification.

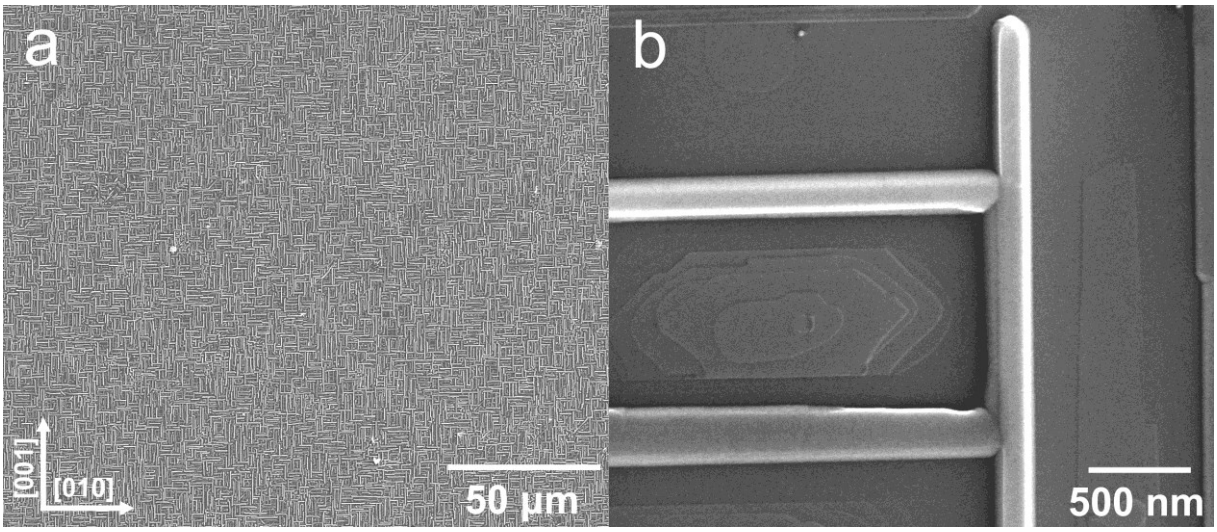

Figure S8. SEM images of a macroscopic TiO nanowire network formed on the surface of $SrTiO_3$. Structure has a high long range order (a), 200 x 200 μm^2), maintaining the perfect crystallinity at the nanoscale (b), 2.5 x 2.5 μm^2).

6. Ways to control nanowires formation

Having presented in the main text of this paper that by the temperature control one can tune the dimensions of the formed TiO nanowires, the main challenge would be to influence the growth at the local scale. Fortunately, the formation of nanowires is correlated with the extended defects in the $SrTiO_3$ matrix. Such defects as dislocations tend often to accumulate into linear agglomerates, oriented along main crystallographic directions. If our growth model is valid, there should be also linear agglomerations of nanowires. To check this experimentally, $SrTiO_3$(100) single crystal surface had been etched for a short time and then an image from optical microscope was collected (Fig. S9 a). It is known that dislocation exits are preferentially etched and pyramidal etch pits are formed [11]. Therefore, apparent lines of etch pits, aligned along main crystallographic directions correspond to the lines of dislocations in STO single crystals. As it was postulated in the main text, dislocations are preferred sites for TiO nanowires growth. It is indeed true and such a structure is presented in Figure S9 b, where a cross-like feature in the nanowire network is observed. The direct proof of the connection between nanowires and dislocations is shown in Figure S9 c, where for the thick enough lamella a feature resembling dislocation with an exit in the TiO nanowire was found.

It is known for decades that the plastic deformation induces a dislocation formation and when the strain is exerted on crystal surface in a linear manner, the resulting dislocations will be also agglomerated linearly. The single crystal cutting is just a procedure that generate

tremendous stress in the vicinity of the cut line, which relaxes and ensues high density of dislocations. The TiO nanowire network formed at the edge of STO is presented in Figure S10. Nanowires, which hitherto have equal probability of be aligned along [010] or [001] directions now are all oriented parallel to the cut edge. It can be directly observed on SEM (Figure S10 b)) and TM-AFM (Figure S10 c)) maps. It provides an opportunity to control the formation of nanowires in terms of their orientation and spacing (nanowire network is now much denser). Summarizing, by the plastic strain engineering one can tailor the metallic nanowires on the perovskite surface.

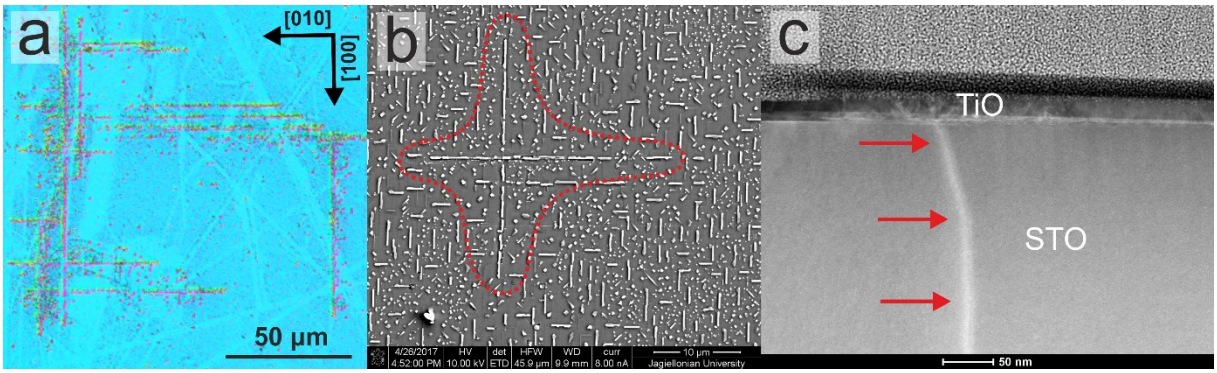

Figure S9. Dislocations impact on TiO nanowires formation. a) Optical image of a $SrTiO_3$(100) surface after etching, showing bands of etch-pits. b) SEM image of a region with cross-like arrangement of nanowires (marked in red), c) HRTEM image of a single TiO nanowire with a dislocation pinned to it.

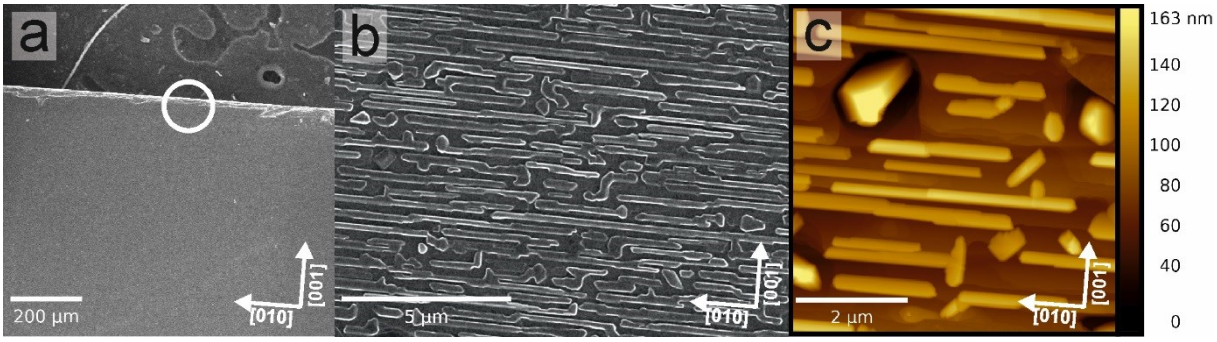

Figure S10. Stress influence on TiO nanowires formation. a) SEM image of a reduced $SrTiO_3$(100) [010] crystal edge, b) SEM image of a zoomed edge area, showing that nearly all of the nanowires are aligned along of the cut direction, c) TM-AFM image of the same area, illustrating that not only all nanowires are grown along horizontal direction but also terrace steps are aligned.

7. TiO nanowires growth model

Here we show a graphical representation of our proposed model regarding initial stages of the TiO nanowires formation on the surface of $SrTiO_3$ due to the thermal reduction. We postulate the transformation of $SrTiO_3$ into network of ordered TiO nanowires is governed by two key processes: incongruent sublimation of strontium and crystallographic shearing. In Figure S11 a side view of the $SrTiO_3(100)$ surface region (blue and yellow atoms stand for oxygen and strontium respectively) is presented.

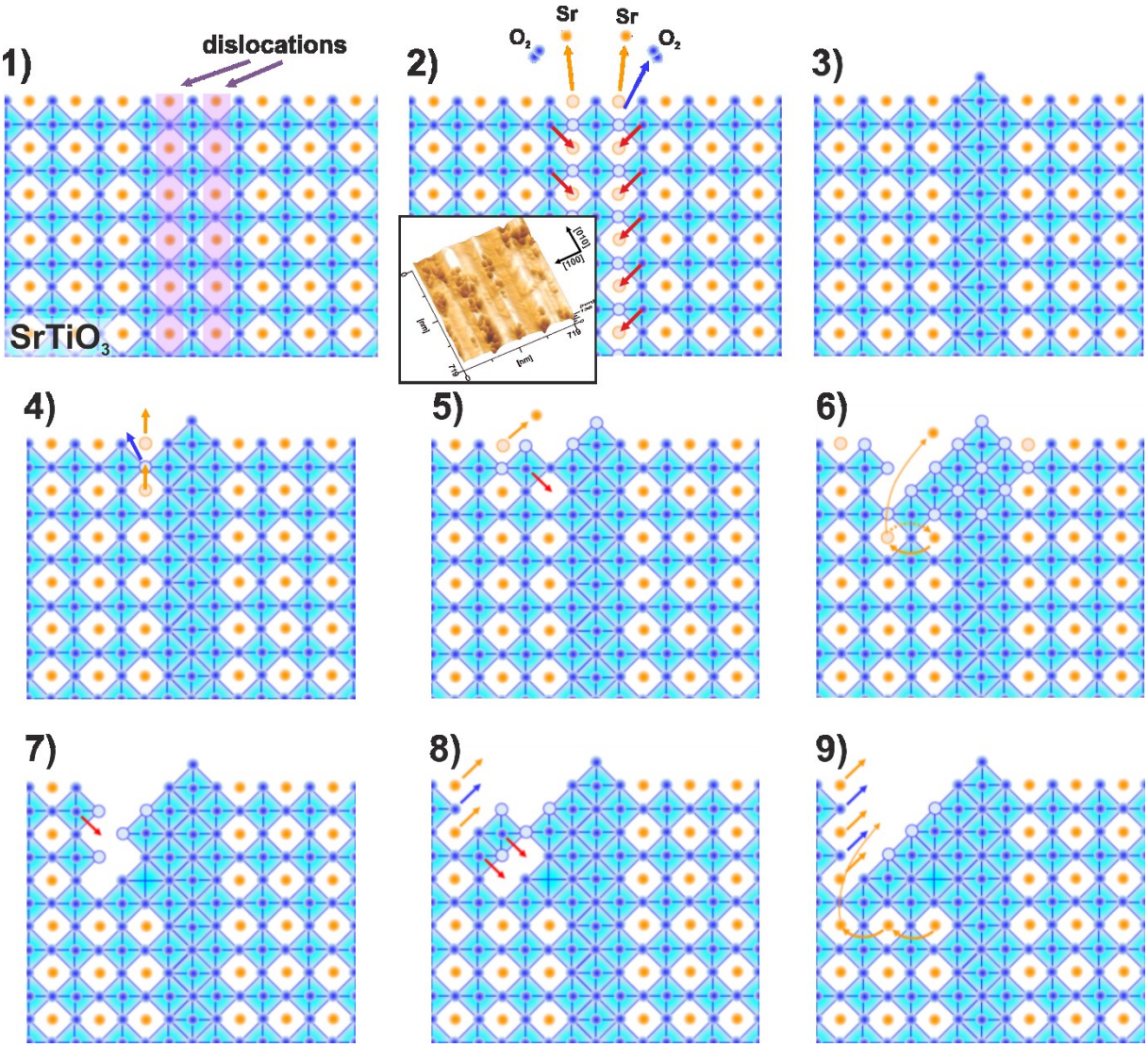

Figure S11. A model explaining the preferred formation of TiO nanowires on the surface of $SrTiO_3(100)$, due to the incongruent sublimation of Sr and crystal decomposition.

1. In the first stage of high-temperature UHV reduction of $SrTiO_3(100)$ crystals an arrangement of reduced edge dislocations is generated. They form of bands along of

the <100> directions (see Fig. S9 a), where a distribution of etch pits on the surface of the reduced $SrTiO_3$ crystal is presented).

2. Under extremely low oxygen partial pressure (utilizing ELOP mechanism with use of the external getter - Si crystal in the experimental realization described in the main text) two processes start along of the dislocations cores: at first a selective sublimation of Sr and removing of O. An effect of such selective decomposition of the crystal close to the dislocation exits is manifested on the topography of the strongly reduced surface layer of $SrTiO_3$, where after heavy thermal reduction pits of tens of nanometers are present (see AFM inset). The easy sublimation of Sr along dislocations on the surface layer of $SrTiO_3$, should be similar to the sublimation of Mg close to the exit of dislocations in MgO [12], This process can be classified as a thermal generation of etch pits. After local depletion of Sr and O a second process takes place, namely a phase transformation of the Sr_0TiO_{3-1} via crystallographic shearing, into anatase TiO_2 and then into TiO with rock salt structure. Notice: it would be difficult to define the sequence of mentioned transformation. It could be that the very strong reduction conditions lead directly in one step to the creation of TiO. Such embedded rocksalt TiO structures were already observed at dislocations cores in $SrTiO_3$ by Buban et al [13].
3. After shearing a TiO nanowire germs with a width of a few lattice constants are created (their crystallographic orientation is <100>). The third stage of the out-of-plane conversion of the $SrTiO_3$ surface layer into TiO is presumably limited to the length of the first segment of dislocations in the hierarchic tree - in our case the depth of the nanowires would be about a few nm.
4. The next phase of the growth of TiO nanowires needs an interplay of the three “sinks for oxygen”: ultrahigh vacuum itself, external getter (here Si) and local getters on the surface of $SrTiO_3$ (here: TiO nanowires edges). We have presented that the annealing of the $SrTiO_3$ in the proximity of TiO leads to the sublimation of Sr [14]. Therefore along of the edge of the TiO nanowires Sr would be much easier removed.
5. After sublimation of Sr atoms close to the edge of a TiO nanowire a row of TiO_{6-x} octahedra is created, which would be subsequently absorbed to existing nanowires using mentioned shearing mechanism. This process causes the in-plane growth of the nanowires. Noteworthy, this kind of transformation of $SrTiO_3$ into titanium suboxides differs than classical growth mechanisms, which would be determined by a free

diffusion of Ti and O. In this case, the shearing would be a more plausible mechanism than the interstitial diffusion of metallic Ti.

6. Images 6-9 present a progress in the in-plane and out-of-plane growth of the TiO nanowires. In principle steps are similar to those, described in points 3-5, with the additional interface mechanism (see Figure 6 and 9). Both figures show a diffusion process of Sr (or SrO) parallel to the interface between nanowires and $SrTiO_3$ crystal. After reaching of the free surface SrO will be incongruently evaporated. This process of conversion of TiO nanowires into the interior of the $SrTiO_3$ crystal along of the interface would only effectively work for a short distance of a few lattice constants. However, since the surface far away from the existing nanowires is also decomposed (due to the ELOP mechanism) causing the Ti(O) enrichment of the surface, nanowires are also expected to absorb material supported by the surface diffusion. This may be proved by a simple observation of TiO nanowires being much higher than the $SrTiO_3$ surface between them. Finally, when nanowires are thick enough, edge dislocations are generated in the TiO crystal, due to the lattices misfit. Those misfit dislocations most likely play an important role in the formation of zig-zag TiO/STO interface, acting as easy diffusion pathways for Sr or SrO [15][16].

1. Drouin, D.; Couture, A. R.; Joly, D.; Tastet, X.; Aimez, V.; Gauvin, R. CASINO V2. 42—A Fast and Easy‐to‐use Modeling Tool for Scanning Electron Microscopy and Microanalysis Users. *Scanning* **2007**, 29(3), 92-101.
2. Tan, H., Verbeeck, J., Abakumov, A., & Van Tendeloo, G. (2012). Oxidation state and chemical shift investigation in transition metal oxides by EELS. Ultramicroscopy, 116, 24-33.
3. Kurata, H., Lefevre, E., Colliex, C., & Brydson, R. (1993). Electron-energy-loss near-edge structures in the oxygen K-edge spectra of transition-metal oxides. Physical Review B, 47(20), 13763.
4. Zhu, G. Z., Radtke, G., & Botton, G. A. (2012). Bonding and structure of a reconstructed (001) surface of SrTiO3 from TEM. Nature, 490(7420), 384.
5. Calvert, C. C., Rainforth, W. M., Sinclair, D. C., & West, A. R. (2006). EELS characterisation of bulk CaCu3Ti4O12 ceramics. Micron, 37(5), 412-419.
6. De Groot, F. M. F., Grioni, M., Fuggle, J. C., Ghijsen, J., Sawatzky, G. A., & Petersen, H. (1989). Oxygen 1s x-ray-absorption edges of transition-metal oxides. Physical Review B, 40(8), 5715.
7. Brydson, R., Sauer, H., Engel, W., & Hofer, F. (1992). Electron energy-loss near-edge structures at the oxygen K edges of titanium (IV) oxygen compounds. Journal of Physics: Condensed Matter, 4(13), 3429.
8. Neish, M. J., Lugg, N. R., Findlay, S. D., Haruta, M., Kimoto, K., & Allen, L. J. (2013). Detecting the direction of oxygen bonding in SrTiO 3. Physical Review B, 88(11), 115120.

9. Wang, Y., Huang, M. R., Salzberger, U., Hahn, K., Sigle, W., & van Aken, P. A. (2018). Towards atomically resolved EELS elemental and fine structure mapping via multi-frame and energy-offset correction spectroscopy. Ultramicroscopy, 184, 98-105.
10. Yamaguchi, A., Haruta, M., Nemoto, T., & Kurata, H. Probing the directionality of local electronic states in SrTiO3 by momentum‐selected STEM‐EELS. In European Microscopy Congress 2016: Proceedings. Wiley‐VCH Verlag GmbH & Co. KGaA.
11. Szot, K., Bihlmayer, G., & Speier, W. (2014). Nature of the Resistive Switching Phenomena in TiO2 and SrTiO3: Origin of the Reversible Insulator–Metal Transition. In Solid State Physics (Vol. 65, pp. 353-559). Academic Press.
12. Yu, Q., Mao, M. M., Li, Q. J., Fu, X. Q., Tian, H., Li, J. X., ... & Zhang, Z. (2016). In Situ Observation on Dislocation-Controlled Sublimation of Mg Nanoparticles. Nano letters, 16(2), 1156-1160.
13. Buban, J. P., Chi, M., Masiel, D. J., Bradley, J. P., Jiang, B., Stahlberg, H., & Browning, N. D. (2009). Structural variability of edge dislocations in a SrTiO 3 low-angle [001] tilt grain boundary. Journal of Materials Research, 24(7), 2191-2199.
14. Rodenbücher, C., Meuffels, P., Speier, W., Ermrich, M., Wrana, D., Krok, F., & Szot, K. (2017). Stability and Decomposition of Perovskite‐Type Titanates upon High‐Temperature Reduction. physica status solidi (RRL)-Rapid Research Letters, 11(9).
15. Paladino, A. E., Rubin, L. G., & Waugh, J. S. (1965). Oxygen ion diffusion in single crystal SrTiO3. Journal of Physics and Chemistry of Solids, 26(2), 391-397.
16. Szot, K., Speier, W., Carius, R., Zastrow, U., & Beyer, W. (2002). Localized metallic conductivity and self-healing during thermal reduction of SrTiO 3. Physical review letters, 88(7), 075508.